# Two-dimensional simulation of Rayleigh waves with staggered sine/cosine transforms and variable grid spacing

Dan Kosloff[1,3] and José M. Carcione[2]

## ABSTRACT

Simulation of Rayleigh waves requires high accuracy and an adequate spatial sampling at the surface. Discrete cosine and sine transforms are used to compute spatial derivatives along the direction perpendicular to the surface of the earth. Unlike the standard Fourier method, these transforms allow nonperiodic boundary conditions to be satisfied, in particular, the stress-free conditions at the surface. Because simulation of surface waves requires more points per minimum wavelength at the surface than simulation of body waves, the equispaced grid is not efficient. To overcome this problem, a grid compression is performed at the surface to obtain a denser spatial sampling. Grid size is minimal at the surface and increases with depth until reaching, at a relatively shallow depth, the grid points per wavelength required by the body waves. The stress-free boundary conditions are naturally handled by expanding the appropriate stress components in terms of the discrete sine transform. The wave equation is solved in the particle-velocity and stress formulation using a Runge-Kutta time integration and the convolutional PML (CPML) method to prevent reflections from the mesh boundaries. The simulations are very accurate for shallow sources and receivers and large offsets.

## INTRODUCTION

Artificially generated surface waves (and particularly Rayleigh waves) are important in various geophysical applications. In geotechnical characterization, use of the Rayleigh wave enables us to estimate the thickness and shear modulus of the surface layer (Gabriels et al., 1987), to predict the lithology ahead of drilling (Bohlen et al., 2007), and to establish seismic microzonation maps (Kind et al., 2005). Malagnini et al. (1995) use Rayleigh waves to determine the anelastic properties of Quaternary layers. Rayleigh waves also are generated naturally by earthquakes. In this case, they are useful to extract information about the structure and properties of the earth at different scales (Knopoff et al., 1966).

Simulation of Rayleigh waves is generally performed by using low-order finite-element and finite-difference (FD) methods (e.g., Levander, 1988). Recent works using finite differences and staggered grids (Mittet, 2002; Bohlen and Saenger, 2006) review the existing methods and propose new approaches to model free-surface boundary conditions. In particular, Bohlen and Saenger (2006) use the so-called image method and compare their results to those of Mittet's heuristic method.

Simulation of the Rayleigh wave requires more points per minimum wavelength than simulation of body waves. This requirement is not only numerical but also due to the fact that the Rayleigh wave is propagating in the horizontal direction but is exponentially damped in the vertical direction. This means that the Rayleigh wave has higher spatial-wavenumber components in the vertical direction (Mittet, 2002). Elastic forward modeling by pseudospectral (PS) methods offers higher accuracy than modeling by FD methods because the differential operator is global, i.e., it uses all the grid points along the direction of differentiation to obtain the derivative. Generally, two grid points per minimum wavelength is enough to model body waves. The drawback is that it is less efficient in terms of computer time compared to FD methods, but this is compensated by the requirement of fewer grid points to discretize the model, mainly in 3D space (e.g., Carcione, 2007).

In addition, unlike with FD methods, it is difficult to implement the free-surface boundary condition with the complex Fourier method because of the spatial periodicity of the derivative operator. A solution to this limitation is offered by Kosloff et al. (1990), where a Chebyshev expansion of the solution is used instead of the Fourier expansion (see Carcione, 2007). See also Carcione (1992), Carcione and Helle (2004), and Carcione et al. (2004) for additional applications of this technique. However, the Chebychev expansion uses a

nonuniform grid that contains more sample points than a regular mesh.

This work presents a new PS modeling scheme in which the variables are expanded in the vertical direction by nonperiodic staggered sine and cosine transforms, which can mathematically handle zero-stress boundary conditions (Press et al., 1992). In the horizontal direction, the solution is expanded by a standard discrete and complex Fourier transform. A grid compression in the vertical direction solves the problem of correct sampling of the surface wave, and use of the convolutional PML (CPML) absorbing-boundary algorithm (e.g., Komatitsch and Martin, 2007) guarantees the absence of artifacts coming from the edges of the mesh.

Moreover, the use of staggered grids with nonlocal differential operators (such as in the pseudospectral method) is important because computation on ordinary uniform grids could cause strong numerical artifacts in the form of noncausal ringing. See Carcione (1999), who solves the viscoelastic equation using the complex version of the staggered Fourier transform.

The algorithm is illustrated with Lamb's problem (a shallow source) and large offsets that require very high accuracy. A typical near-surface example is simulated.

## THE WAVE EQUATION

The 2D particle-velocity-stress equations for elastic propagation in the $x$-$y$ plane can be expressed by (e.g., Carcione, 2007)

1. Newton's equations:

$$\sigma_{xx,x} + \sigma_{xz,z} = \rho\dot{v}_x + f_x,$$
$$\sigma_{xz,x} + \sigma_{zz,z} = \rho\dot{v}_z + f_z, \tag{1}$$

where $v_x$ and $v_z$ are the particle velocities, $\sigma_{xx}$, $\sigma_{zz}$, and $\sigma_{xz}$ are the stress components, $\rho$ is the density, and $f_x$ and $f_z$ are the body forces. A dot above a variable denotes time differentiation and a subindex after a comma indicates spatial differentiation.

2. Constitutive equations:

$$\dot{\sigma}_{xx} = c_{11}v_{x,x} + c_{13}v_{z,z},$$
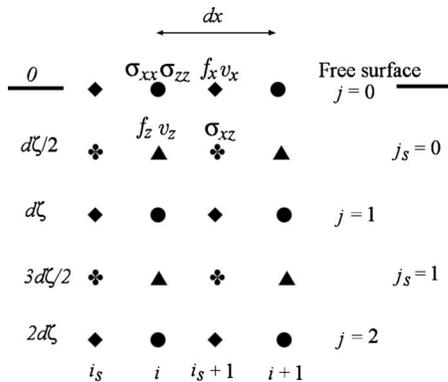$$\dot{\sigma}_{zz} = c_{13}v_{x,x} + c_{33}v_{z,z},$$



Figure 1. Equispaced numerical mesh used to compute staggered differential derivatives and implement free-surface boundary conditions. Regular grid points are denoted by $(i, j)$ (full circles), and staggered grid points by $(i_s, j_s)$; $dx$ and $d\zeta$ indicate the grid spacing. A grid compression is applied to this mesh to reduce grid spacing at the surface.

$$\dot{\sigma}_{xz} = c_{55}(v_{x,z} + v_{z,x}), \tag{2}$$

where $c_{IJ}$ are the elastic constants.

In this work, we consider an isotropic medium ($c_{13} = c_{11} - 2c_{55}$ and $c_{33} = c_{11}$), but the algorithm is valid for a transversely isotropic solid with its symmetry axis perpendicular to the surface of the earth (VTI medium) in the case that no constraints, other than stability, are imposed on $c_{13}$ and $c_{33}$.

## STAGGERED MESH

On a regular grid, all the field components and material properties are represented at the same grid point. On a staggered grid, the field variables are defined at grid points and at half-grid points, as indicated in the mesh shown in Figure 1. Material properties are defined at the grid points corresponding to the following variables:

$$(i,j) = (i,j)\sigma_{xx}, \sigma_{zz}, c_{11}, c_{33}, c_{13},$$

$$(i_s,j) = \left(i \pm \frac{1}{2}, j\right)v_x, f_x, \rho,$$

$$(i,j_s) = \left(i, j \pm \frac{1}{2}\right)v_z, f_z, \rho,$$

$$(i_s,j_s) = \left(i \pm \frac{1}{2}, j \pm \frac{1}{2}\right)\sigma_{xz}, c_{55}. \tag{3}$$

The grid spacings are $dx$ and $d\zeta$ along the horizontal and vertical directions, respectively. A grid compression is applied in the vertical direction, implying a variable grid spacing near the surface with a minimum grid size $dz < d\zeta$ (see below).

Material properties at half-grid points are computed by averaging the values defined at regular points. The averaging is chosen in such a way to reduce the error between the numerical solution corresponding to an interface aligned with the numerical grid and the equivalent solution obtained with a regular grid. Minimum ringing amplitudes for the example illustrated in the next section are obtained when the averages are computed as follows (Røsten et al., 1996). Density is averaged as

$$\rho^{i+\frac{1}{2},j} = \frac{1}{2}(\rho^{i,j} + \rho^{i+1,j}) \text{ and } \rho^{i,j+\frac{1}{2}} = \frac{1}{2}(\rho^{i,j} + \rho^{i,j+1}), \tag{4}$$

and $c_{55}$ as

$$\left(c_{55}^{i+\frac{1}{2},j+\frac{1}{2}}\right)^{-1} = \frac{1}{4}[(c_{55}^{i,j})^{-1} + (c_{55}^{i+1,j})^{-1} + (c_{55}^{i,j+1})^{-1}$$
$$+ (c_{55}^{i+1,j+1})^{-1}]. \tag{5}$$

On the other hand, the alternative averaging performed by Mittet (2002) can be used (i.e., arithmetic averages for density and shear modulus). He tries several averaging schemes for the density, but they all lead to numerical artifacts even for plane interfaces, especially if the source is placed close to the interface. The interface appears to have a saw-edge behavior if density averaging is not performed properly.

## CALCULATION OF SPATIAL DERIVATIVES

The real sine and cosine discrete Fourier transforms (DST and DCT) can be used to solve differential equations with spectral accuracy and nonperiodic boundary conditions. Moreover, these transforms can handle common boundary conditions of their functions naturally, i.e., they have the value zero at the boundaries or their derivatives are zero at the boundaries. In the first instance, the natural transform to use is the sine transform. In the second case, it is the cosine transform. The DCT-I and DST-I compute the transforms of functions sampled at regular grid points, and DCT-II and DST-II compute the transforms of functions sampled at half-grid points. The DST/DCT transforms are used here for expanding the solution in the vertical direction. Calculation of derivatives in the horizontal direction is carried out with a staggered discrete Fourier expansion (see Carcione, 1999, 2007), satisfying periodic boundary conditions.

For a function with values given on regular grid points, the sine expansion is

$$f(x_j) = \sum_{i=1}^{N-1} F_i \sin(k_i x_j), \quad k_i = \frac{i\pi}{Ndx} \text{ and } x_j = jdx,$$
$$j = 1,\ldots,N-1, \tag{6}$$

where $dx$ is the grid spacing and $F_i$ are calculated by the DST-I:

$$F(k_i) = \frac{2}{N} \sum_{j=1}'^{N-1} f_j \sin(k_i x_j). \tag{7}$$

The corresponding cosine expansion is

$$f(x_j) = \sum_{i=0}'^{N} F_i \cos(k_i x_j), \quad k_i = \frac{i\pi}{Ndx} \text{ and } x_j = jdx,$$
$$j = 0,\ldots,N, \tag{8}$$

where $F_i$ are calculated by the DCT-I:

$$F(k_i) = \frac{2}{N} \sum_{j=0}'^{N} f_j \cos(k_i x_j). \tag{9}$$

A prime on the summation symbol means that the terms for $j = 0$ and $j = N$ have a coefficient $\frac{1}{2}$ in front.

For a function with values given on half grid points, the sine expansion is

$$f\left(x_j + \frac{dx}{2}\right) = \frac{2}{N} \sum_{i=1}^{N} F_i \sin\left[k_i\left(x_j + \frac{dx}{2}\right)\right],$$
$$j = 0,\ldots,N-1, \tag{10}$$

where $F_i$ are calculated by the DST-II:

$$F(k_i) = \sum_{j=0}^{N-1} f_j \sin\left[k_i\left(x_j + \frac{dx}{2}\right)\right]. \tag{11}$$

The corresponding cosine expansion is

$$f\left(x_j + \frac{dx}{2}\right) = \frac{2}{N} \sum_{i=0}'^{N-1} F_i \cos\left[k_i\left(x_j + \frac{dx}{2}\right)\right],$$
$$j = 0,\ldots,N-1, \tag{12}$$

where $F_i$ are calculated by the DCT-II:

$$F(k_i) = \sum_{j=0}^{N-1} f_i \cos\left[k_i\left(x_j + \frac{dx}{2}\right)\right]. \tag{13}$$

For instance, the staggered derivative of equation 8 is given by

$$\frac{\partial f}{\partial x}\left(x_j + \frac{dx}{2}\right) = \sum_{i=0}^{N-1} G_i \sin\left[k_i\left(x_j + \frac{dx}{2}\right)\right], \tag{14}$$

where $G_i = -k_i F_i$. The calculation is performed by first computing $F_i$ by a DCT-I on $f$, then calculating $G_i$ and an inverse DST-II to get the derivative. The staggered derivative of equation 6 at $x_j$ is calculated in a similar manner with a DST-II, calculation of $F_i = k_i G_i$, and an inverse DCT-I.

## COORDINATE COMPRESSION

Mittet (2002) shows that the Rayleigh wave cannot be sampled properly with two grid points per shortest wavelength if the shortest wavelength is calculated as the Rayleigh-wave velocity divided by the maximum frequency. This is because the Rayleigh wave is a propagating wave parallel to the free surface, but exponentially damped away from the free surface. This damping of the Rayleigh wave generates high spatial wavenumbers in the wavefield, and denser sampling is required at the free surface in the vertical direction. This is well accomplished by the Chebyshev method when computing the derivatives along the vertical direction (Kosloff et al., 1990) because the Gauss-Lobatto points are denser at the boundaries of the grid.

Here we use a coordinate compression at the surface to obtain a variable grid spacing. We consider the mapping function

$$z(\zeta) = \left(\frac{1+\alpha}{2}\right)\zeta - \left(\frac{1-\alpha}{2}\right)\frac{\zeta_0}{\pi} \sin\left(\frac{\pi\zeta}{\zeta_0}\right), \tag{15}$$

where $\zeta$ is the vertical coordinate in the equispaced mesh, $\zeta_0$ is a given vertical distance in that mesh, and $\alpha$ is the compression factor. If $d\zeta$ is the original grid spacing, then $dz = z(d\zeta) - z(0) \approx \alpha d\zeta$, i.e., if $\alpha = 0.5$, the grid spacing is reduced by half at the surface. If $\zeta = \zeta_0$, the physical distance is $z_0 = (1+\alpha)/2$ and the grid spacing at and below $z_0$ is $d\zeta$.

The derivative of a field variable is calculated by the chain rule

$$\frac{\partial f}{\partial z} = \frac{\partial f}{\partial \zeta} \cdot \frac{d\zeta}{dz}, \tag{16}$$

where

$$\frac{dz}{d\zeta} = \left(\frac{1-\alpha}{2}\right)\left[1 - \cos\left(\frac{\pi\zeta}{\zeta_0}\right)\right] + \alpha. \tag{17}$$

## STRESS-FREE BOUNDARY CONDITIONS

The free-surface boundary conditions are

$$\sigma_{xz}^{\text{new}} = \sigma_{zz}^{\text{new}} = 0, \tag{18}$$

at $j = 0$ as indicated in Figure 1, where superindices "new" and "old" (see below) indicate the new and old values of the fields after and before the imposition of the boundary conditions, respectively. The staggered index $j_s$ is represented by an integer number in pro-

gramming. Vertical derivatives of $v_x$ and $v_z$ are calculated by DCT-I/DST-II and DST-II/DCT-I expansions, and vertical derivatives of $\sigma_{xz}$ and $\sigma_{zz}$ are calculated by DST-II/DCT-I and DST-I/DCT-II expansions, respectively. However, the condition $\sigma_{zz}^{new} = 0$ is equivalent to replacing $v_{z,z}^{old}$ by $v_{z,z}^{old} - c_{33}^{-1}\dot{\sigma}_{zz}^{old}$ (see equations 2). Then, we have to modify $\sigma_{xx}$ at the surface using the following equation:

$$\sigma_{xx}^{new} = \sigma_{xx}^{old} - \frac{c_{13}}{c_{33}}\sigma_{zz}^{old}, \quad \text{at } j = 0. \quad (19)$$

(The modification is performed at the same time step.) Conditions 18 are satisfied because the stress components are represented by sine expansion and therefore their values are zero at the surface. One may argue that $v_z = 0$ at the free surface because of the expansion DST-II. However, the value is effectively modified there, after enforcing the boundary conditions $\sigma_{zz}^{new} = 0$. Actually, we do not take the value of $v_{z,z}^{new}$ from the DST-II/DCT-I calculation, but we effectively set $v_{z,z}^{new} = -(c_{13}/c_{33})v_{x,x}^{old}$ (from $\sigma_{zz}^{new} = 0$ at $z = 0$).

We impose rigid boundary conditions at the bottom.

## CPML ABSORBING BOUNDARIES

We use the last version of the PML method to absorb unphysical reflections from the edges of the mesh. It is the unsplit convolutional PML method or CPML (e.g., Komatitsch and Martin, 2007). Inside the PML strips, each of the spatial derivatives in equations 1 and 2 are replaced by a time convolution

$$\partial_i f \rightarrow s * \partial_i f, \quad i = x, z, \quad (20)$$

where

$$s(t) = \frac{\delta(t)}{\kappa} + a \exp(-bt)H(t). \quad (21)$$

Time convolution is denoted by $*$, $H$ is the step function, $\delta$ is the Dirac function, and $\kappa$, $a$, and $b$ are absorbing parameters.

Let us transform the convolution into a differential equation. Note that

$$s = \frac{\delta}{\kappa} + gH, \quad g = a \exp(-bt), \quad \dot{g} = -bg. \quad (22)$$

We have

$$s * \partial_i f = \frac{\partial_i f}{\kappa} + e_f, \quad e_f = gH * \partial_i f, \quad (23)$$

where $e_f$ is a memory variable. The idea of using memory variables is similar to that used in numerical modeling in geophysics to implement viscoelasticity in the seismic wave equation (Carcione et al., 1988).

The time derivative of the memory variable is

$$\dot{e}_f = (\delta g + \dot{g}H) * \partial_i f = g(0)\partial_i f - bgH * \partial_i f$$
$$= g(0)\partial_i f - be_f, \quad (24)$$

or

$$\dot{e}_f = a\partial_i f - be_f. \quad (25)$$

There are eight distinct spatial derivatives in equations 1 and 2. These are modified inside the absorbing strips only. Each derivative

$\partial_i f$ is replaced by $(\partial_i f)/\kappa + e_f$ and the additional differential equation $\dot{e}_f = a\partial_i f - be_f$ has to be solved. This equation is slightly different from that obtained by Komatitsch and Martin (2007). However, both equations are equivalent for the time step used in the numerical calculations ($dt$ is small enough) and the performance is the same. This is shown in the following. Using our notation, equation 26 of Komatitsch and Martin (2007) can be written as

$$e_f^{n+1} = \left[ e_f^n - \frac{a}{b}(\partial_i f)^{n+1/2} \right] \exp(-bdt) + \frac{a}{b}(\partial_i f)^{n+1/2}, \quad (26)$$

where $n$ denotes the $n$-th time step. Because $\exp(-bdt) \approx 1 - bdt$, we obtain

$$e_f^{n+1} = e_f^n + dt[a(\partial_i f)^{n+1/2} - be_f^n], \quad (27)$$

which is precisely the first-order time discretization of equation 25.

Assume the $x$-direction. According to Komatitsch and Martin (2007), $\kappa = 1$,

$$a = \frac{3v_p \ln(0.001)(i-1)^2 dx^2}{2L^3}, \quad i = 1, \dots, N, \quad (28)$$

$$b = -\frac{\pi f_p (i-N)dx}{L} - a, \quad (29)$$

where $N$ is the number of points of the strip, $L = (N-1)dx$ is the length of the strip, $dx$ is the grid spacing, $v_p$ is the phase velocity, and $f_p$ is the source peak frequency.

## TESTS AND GEOPHYSICAL EXAMPLE

We compare numerical and analytical solutions for Lamb's problem. The latter solution is obtained by the method of Cagniard-De Hoop (Berg et al., 1994). To compute the transient responses, we use as a source a Ricker time history of the form

$$h(t) = \left( \theta - \frac{1}{2} \right) \exp(-\theta), \quad \theta = \left[ \frac{\pi(t-t_s)}{t_p} \right]^2, \quad (30)$$

where $t_p$ is the period of the wave (the distance between the side peaks is $\sqrt{6}t_p/\pi$) and we take $t_s = 1.4t_p$. Its frequency spectrum is

$$H(\omega) = \left( \frac{t_p}{\sqrt{\pi}} \right) \bar{\theta} \exp(-\bar{\theta} - i\omega t_s), \quad \bar{\theta} = \left( \frac{\omega}{\omega_p} \right)^2,$$

$$\omega_p = \frac{2\pi}{t_p}. \quad (31)$$

The peak frequency is $f_p = 1/t_p$ and the cut-off frequency is $2f_p$.

The material properties are $c_{11} = c_{33} = \rho v_P^2 = 8.8$ GPa, $c_{13} = 2.93$ GPa, $c_{55} = \rho v_S^2 = c_{11}/3 = 2.93$ GPa, and $\rho = 2.2$ g/cm³, which give the P- and S-wave velocities $v_P = 2000$ m/s and $v_S = v_P/\sqrt{3} = 1155$ m/s, respectively. We take $f_p = 15$ Hz and consider a mesh with grid points $N_x = N_z = 264$, $dx = 10$ m, and $d\zeta = 5$ m. For the first test, we consider an equispaced grid, i.e., there is no grid compression ($\alpha = 1$). The source is a vertical force $f_z$ located at grid point (100,2), i.e., at a depth of 7.5 m, and the receivers are placed at grid point (170,2). This means (695,5) m for $v_x$ and (700,7.5) m for $v_z$, relative to the source (see a more detailed expla-

nation below to properly locate the fields in a staggered grid). The time-stepping method used for the simulations is a fourth-order Runga-Kutta algorithm (e.g., Carcione, 2007). At the sides and bottom of the mesh, there are strips of a length of 20 grid points to implement the CPML absorbing conditions. The solution is obtained with a time step $dt = 0.25$ ms. Figure 2 compares the numerical and analytical solutions, where it can be seen that the match is not good. In this case, the number of points per dominant Rayleigh wavelength ($v_R/(f_p d\zeta)$) is approximately 14 (seven points per minimum wavelength), based on a (Poisson's solid) Rayleigh-wave velocity $v_R \approx 0.92 v_S$. On the other hand, the P-wave is correctly simulated, with points per dominant P-wavelength equal to 13 if we consider horizontal grid spacing and 26 if we consider vertical grid spacing.

Now let us consider a variable grid spacing at the surface and more challenging conditions, i.e., shallower location of source and receivers. Compression parameters are $\alpha = 0.1$, so that $dz = 0.5$ m at the surface and $\zeta_0/d\zeta = 50$. Then, the first 250 m in the equispaced mesh are compressed to 137.5 m in the physical mesh. The

source is located at the grid point $(i, j_s) = (100, 5)$, and two receivers R1 and R2 record the field at grid points $(i_s, j) = (170, k)$ for $v_x$ and $(i, j_s) = (170, k)$ for $v_z$, where $k = 2$ (R1) and $k = 83$ (R2). For the comparison, one has to correctly compute locations of the source and receiver for calculation of the analytical solution. Let us consider receiver R1. Taking Figure 1 as a reference, the location of the source is $(0, 22.5)$ m in the equispaced grid and $(0, 2.38)$ m in the physical grid because $j_s = 5$. The receivers are located at $(695, 0.75)$ m for $v_x$ and $(700, 1)$ m for $v_z$ (physical grid) because for these, $i_s = i - \frac{1}{2}$ and $j_s = 5$, respectively. Then, the actual location of the vertical force (in the equispaced grid) is $\left(k - \frac{1}{2}\right) d\zeta$, and the location of the horizontal force is $k d\zeta$. Compression mapping gives the physical locations through equation 15. Receiver R2 has the following locations in the physical space: $(695, 297.5)$ m for $v_x$ and $(700, 300)$ m for $v_z$. The comparison for R1 is shown in Figure 3. As can be appreciated, the match is very good. Figure 4 shows a comparison at a depth of 300 m. In this case, the agreement is excellent. Using the same medium properties and modeling parameters, we consider an offset of 1.4 km. The comparison for the shallow re-
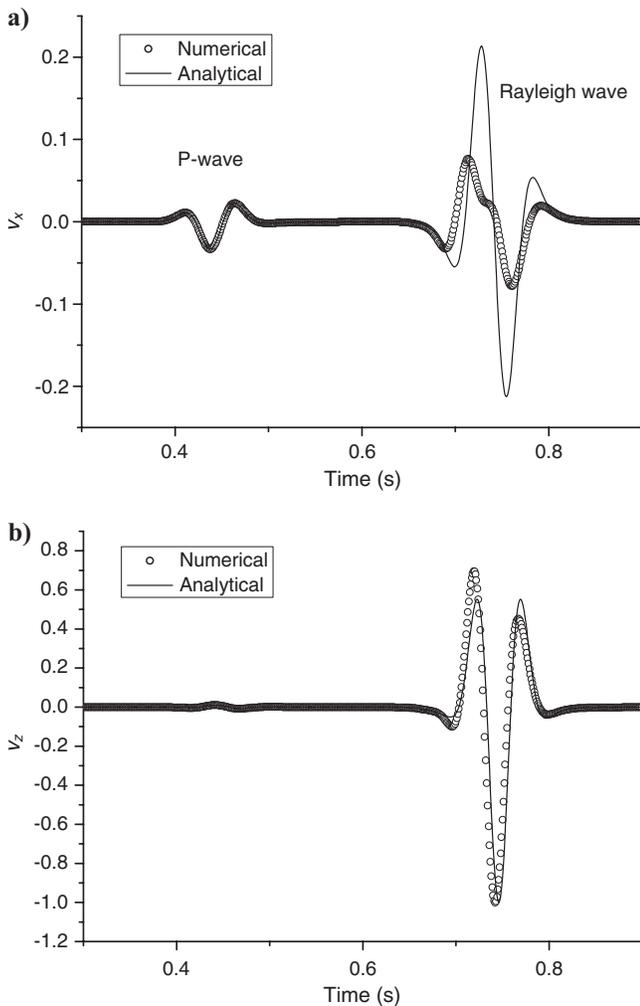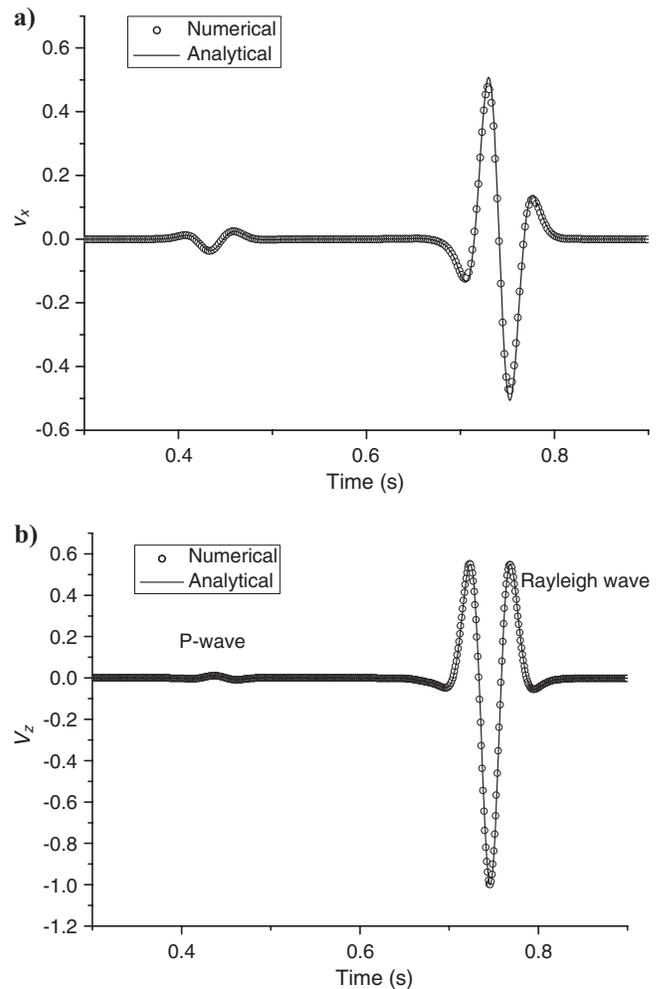


Figure 2. Comparison between the numerical and analytical solutions for a source-receiver distance of 700 m; (a) and (b) correspond to the horizontal and vertical particle-velocity components, respectively, normalized with respect to the maximum value of $v_z$. There is no compression of grid points at the surface ($\alpha = 1$), source depth is 7.5 m, and receiver depth is 5 m for $v_x$ and 7.5 $m$ for $v_z$.

Figure 3. Comparison between the numerical and analytical solutions for a source-receiver distance of 700 m; (a) and (b) correspond to the horizontal and vertical particle-velocity components, respectively, normalized with respect to the maximum value of $v_z$. The compression factor is $\alpha = 0.1$, source depth is 2.38 m, and receiver depth is 0.75 m for $v_x$ and 1 m for $v_z$.

ceiver is shown in Figure 5, where we can see that the agreement is still satisfactory for practical purposes. Numerical experiments with $d\zeta = 10$ m and a compression factor $\alpha = 0.1$ show that the results are equally satisfactory. In this case, grid spacing at the surface is 1 m and the points per minimum wavelength computed on the basis of this grid spacing are approximately 35. The use of fewer points than this limit does not provide a good agreement between solutions.

As we have seen, the algorithm performs well on a single-trace basis and this makes it reliable for practical applications. The classical example in near-surface geophysics is the simulation of ground roll. This is caused by the presence of a shallow low-velocity layer, usually called the weathering layer. Let us assume the medium properties of the previous tests for a shallow layer of 140 m thickness and two cases as indicated in Figure 6, where the geological model is shown. (The S-wave velocity is given by $v_P/\sqrt{3}$.) Seismograms corresponding to the vertical particle velocities are shown in Figure 7a and b, and a snapshot of the vertical particle velocity for case A is displayed in Figure 8. When the surface layer has a low velocity (case A), the Rayleigh wave is dispersive and ground roll is generated. On the oth-

er hand, when there is an inversion in the seismic velocity (case B), ground roll is not present. This occurs, for instance, in the earth poles, where a high-velocity layer (ice) overlies a low-velocity layer (permafrost), or on land, when there is a basalt layer at the surface. There are no trapped modes in these cases, because P- and S-waves
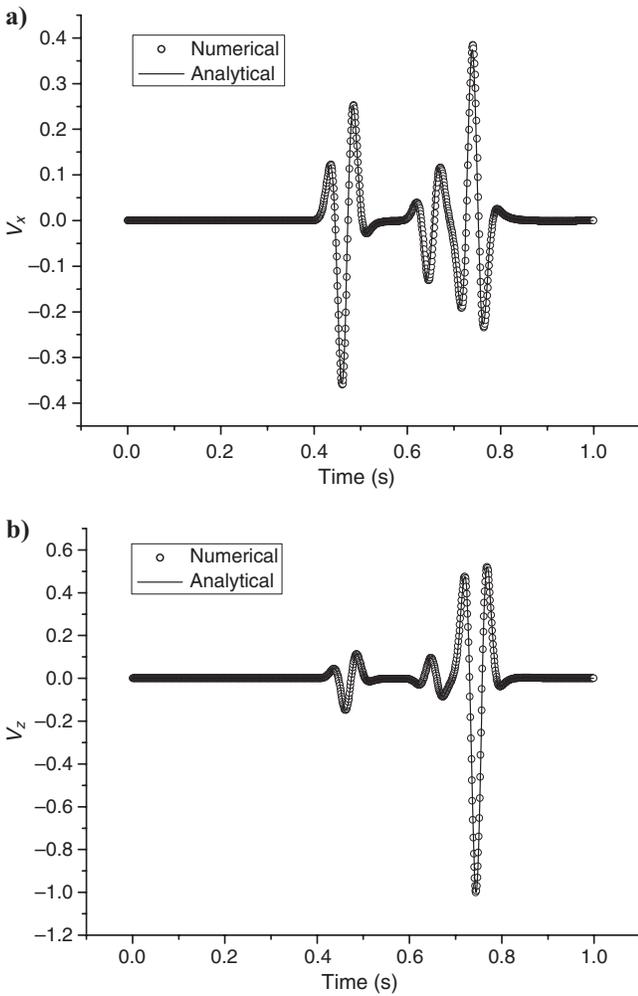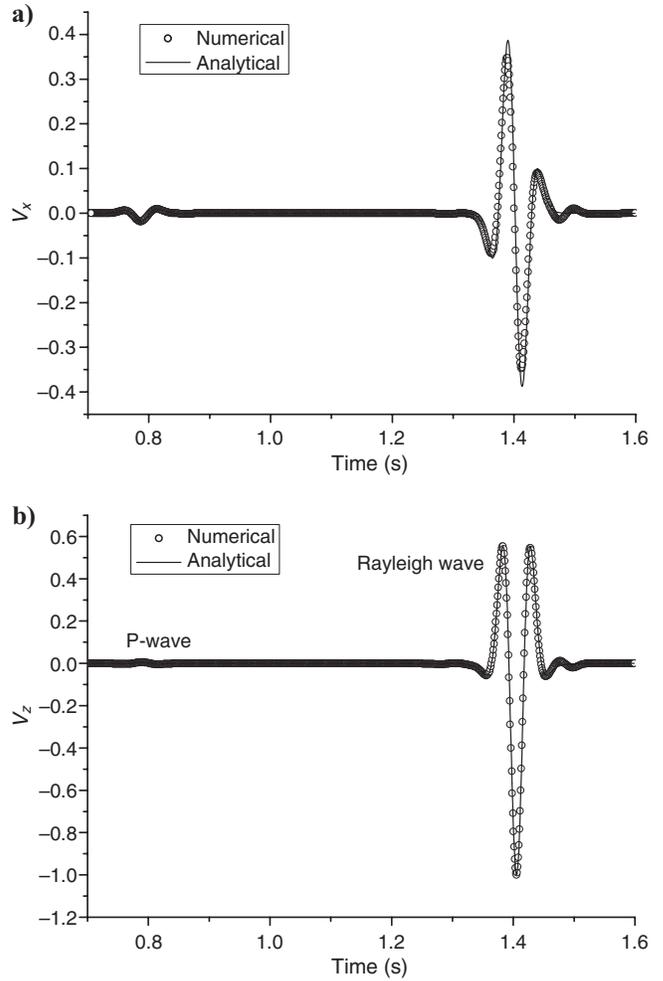
**a)**

**b)**

Figure 5. Comparison between the numerical and analytical solutions for a source-receiver distance of 1400 m; (a) and (b) correspond to the horizontal and vertical particle-velocity components, respectively, normalized with respect to the maximum value of $v_z$. The compression factor is $\alpha = 0.1$, source depth is 2.38 m, and receiver depth is 2.09 m for $v_x$ and 2.38 m for $v_z$.

**a)**

**b)**

Figure 4. Comparison between the numerical and analytical solutions for a source-receiver distance of 700 m; (a) and (b) correspond to the horizontal and vertical particle-velocity components, respectively, normalized with respect to the maximum value of $v_z$. The compression factor is $\alpha = 0.1$, source depth is 2.38 m, and receiver depth is 297.5 m for $v_x$ and 300 m for $v_z$.
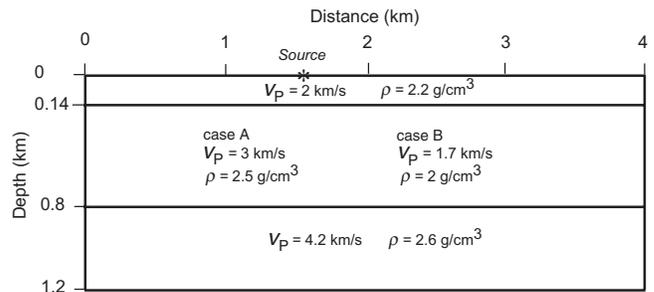
Figure 6. Geologic model, where P-wave velocity and density of the layers are indicated. The S-wave velocity is given by $v_S = v_P/\sqrt{3}$. Two cases are considered: case A for hard layers and case B for soft layers compared to the overlying surface properties.

are not evanescent in the half space when its wave velocity is lower than that of the layer. In mathematical terms, Mooney and Bolt (1966) show that when $v_S$ (half-space) $<v_S$ (layer), the roots of the dispersion equation are all complex unless that of the fundamental mode.

Strong lateral variations of the near-surface properties can be handled appropriately by pseudospectral methods, such as the present method. Examples can be found in Carcione (1992), Priolo et al.
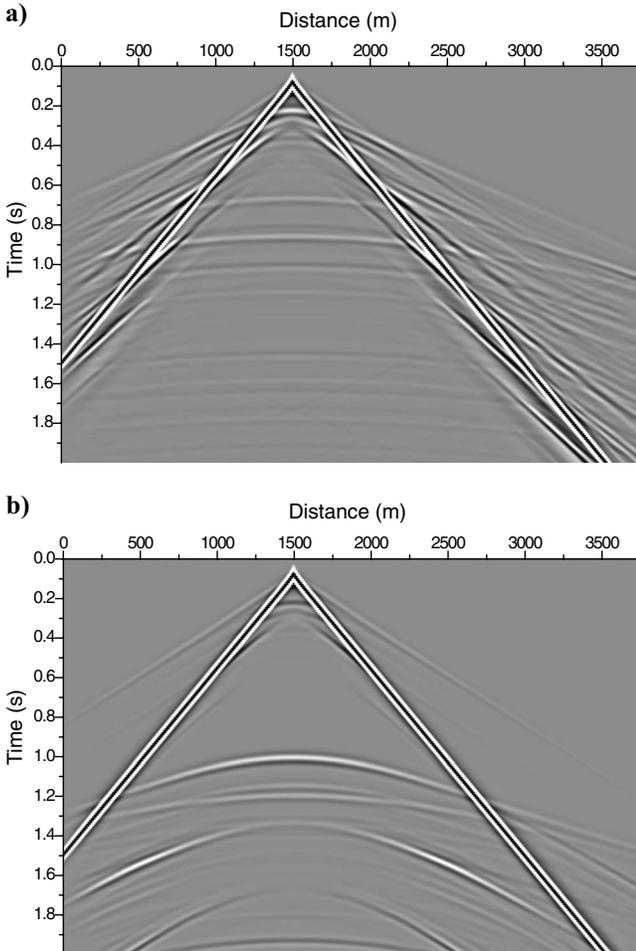
**a)**



**b)**



Figure 7. The $v_z$ seismograms corresponding to cases A and B for the simulation of Rayleigh surface waves. The model is shown in Figure 6. The dispersed Rayleigh wave (ground roll) can be seen clearly as a high-amplitude (linear) event with a traveltime of 1.4 s at a horizontal distance of 0 m.
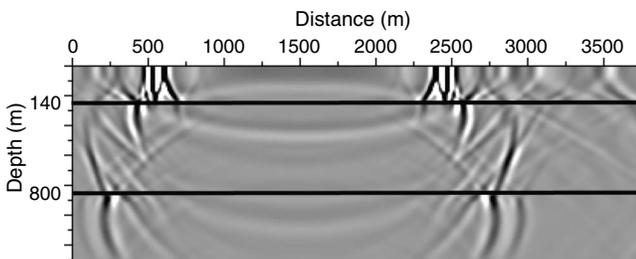


Figure 8. The $v_z$ snapshots at $t = 1$ s for case A. The model is shown in Figure 6. The dispersed Rayleigh waves (ground roll) can be seen at the horizontal distances of 500 and 2500 m.

(1994), and Carcione et al. (2004), where a vertical interface touching the free surface with large property contrasts is considered.

## CONCLUSIONS

It is already well established that simulation of seismic Rayleigh waves (and surface waves in general) requires more grid points per minimum wavelength than simulation of body waves, mainly when the source and receivers are close to the surface (less than 2 or 3 m) and offsets are large, say, exceeding 500 m. Dense grid spacing in the vertical direction is achieved by using a compression mapping in a region close to the surface, and spatial derivatives are computed using staggered pseudospectral cosine and sine transforms, which guarantee the use of a coarse grid in the interior of the mesh. These transforms require half the grid points used by the Chebyshev differential operator, which is also based on the fast Fourier transform. (Memory storage is reduced approximately by half.) This implies the best discretization for pseudospectral methods in the presence of free-surface conditions. Because the grid compression is performed at a zone near the surface, reduction of the model along the vertical direction is minimal. Therefore, the proposed algorithm is highly accurate and can handle the propagation of Rayleigh waves at large offsets. This is important for application to near-surface problems and earthquake seismology.

Further research involves analysis of the performance of alternative free-surface methods using the present numerical solver, as the image method or Mittet's heuristic approach. Moreover, extension of the algorithm to three dimensions is required to model Love waves. In this case, the number of grid points per wavelength used here should be appropriate because Love waves propagate at a shear-wave velocity that is slightly larger than Rayleigh-wave velocity. Grid compression is required only near the surface along the vertical direction, and therefore the 3D extension is straightforward. Finally, the modeling is also suitable to model Scholte waves (at fluid-solid interfaces), which can be implemented by domain-decomposition methods, as previously performed by the authors using Chebyshev spatial differentiation.

## ACKNOWLEDGMENTS

## REFERENCES

Berg, P., F. If, P. Nielsen, and O. Skovgaard, 1994, Analytical reference solutions, *in* K. Helbig, ed., Modeling the earth for oil exploration: Pergamon, 421–427.

Bohlen, T., U. Lorang, W. Rabbel, C. Müller, R. Giese, S. Lüth, and S. Jetschny, 2007, Rayleigh-to-shear wave conversion at the tunnel face — From 3D-FD modeling to ahead-of-drill exploration: Geophysics, **72**, no. 6, T67–T79.

Bohlen, T., and E. H. Saenger, 2006, Accuracy of heterogeneous staggered-grid finite-difference modeling of Rayleigh waves: Geophysics, **71**, no. 4, T109–T115.

Carcione, J. M., 1992, Modeling anelastic singular surface waves in the earth: Geophysics, **57**, 781–792.

——, 1999, Staggered mesh for the anisotropic and viscoelastic wave equation: Geophysics, **64**, 1863–1866.

——, 2007, Wave fields in real media: Theory and numerical simulation of wave propagation in anisotropic, anelastic, porous and electromagnetic media, second edition: Elsevier.

Carcione, J. M., and H. B. Helle, 2004, On the physics and simulation of wave propagation at the ocean bottom: Geophysics, **69**, 825–839.

Carcione, J. M., D. Kosloff, and R. Kosloff, 1988, Viscoacoustic wave propa-

gation simulation in the earth: Geophysics, **53**, 769–777.

Carcione, J. M., F. Poletto, and D. Gei, 2004, 3D wave simulation in anelastic media using the Kelvin-Voigt constitutive equation: Journal of Computational Physics, **196**, 282–297.

Gabriels, P., R. Snieder, and G. Nolet, 1987, In situ measurements of shear-wave velocity in sediments with higher-mode Rayleigh waves: Geophysical Prospecting, **35**, 187–196.

Kind, F., D. Fäh, and D. Giardini, 2005, Array measurements of S-wave velocities from ambient vibrations: Geophysical Journal International, **160**, 114–126.

Knopoff, L., S. Mueller, and W. L. Pilant, 1966, Structure of the crust and upper mantle in the Alps from the phase velocity of Rayleigh waves: Bulletin of the Seismological Society of America, **56**, 1009–1044.

Komatitsch, D., and R. Martin, 2007, An unsplit convolutional perfectly matched layer improved at grazing incidence for the seismic wave equation: Geophysics, **72**, no. 5, SM155–SM167.

Kosloff, D., D. Kessler, A. Queiroz Filho, E. Tessmer, A. Behle, and R. Strahilevitz, 1990, Solution of the equations of dynamic elasticity by a Chebychev spectral method: Geophysics, **55**, 734–748.

Levander, A., 1988, Fourth-order finite-difference P-SV seismograms: Geo-

physics, **53**, 1425–1436.

Malagnini, L., R. B. Herrmann, G. Biella, and R. de Franco, 1995, Rayleigh waves in Quaternary alluvium from explosive sources: Determination of shear-wave velocity and Q structure: Bulletin of the Seismological Society of America, **85**, 900–922.

Mittet, R., 2002, Free-surface boundary conditions for elastic staggered-grid modeling schemes: Geophysics, **67**, 1616–1623.

Mooney, H. M., and B. A. Bolt, 1966, Dispersive characteristics of the first three Rayleigh modes for a single surface layer: Bulletin of the Seismological Society of America, **56**, 43–67.

Press, W. H., S. A. Teukolsky, W. T. Vetterling, and B. P. Flannerty, 1992, Numerical recipes in C: The art of scientific computing, second edition: Cambridge University Press.

Priolo, E., J. M. Carcione, and G. Seriani, 1994, Numerical simulation of interface waves by high-order spectral modeling techniques: Journal of the Acoustical Society of America, **95**, 681–693.

Røsten, T., L. Amundsen, B. Arnsten, and Å. Kristensen, 1996, Finite-difference modelling with application to interface wave propagation: Third European Conference on Underwater Acoustics, Proceedings, 315–320.